Summer Convective Precipitation Changes over the Great Lakes Region under a Warming Scenario

Zhao Yang[1], Jiali Wang[2], Yun Qian[1*], TC Chakraborty[1], Pengfei Xue[2,3], William J. Pringle[2], Chenfu Huang[3], Miraj Bhakta Kayastha[3], Huilin Huang[1], Jianfeng Li[1], Robert Hetland[1]

[1] Pacific Northwest National Laboratory, Richland, Washington, USA

[2] Environmental Science Division, Argonne National Laboratory, Lemont, IL, USA.

[3] Department of Civil, Environmental and Geospatial Engineering, Michigan Technological University, Houghton, MI, USA.

Corresponding author: Zhao Yang (zhao.yang@pnnl.gov); Yun Qian (yun.qian@pnnl.gov)

Key Points:

- The location of summer convective precipitation is shifted due to global and regional warming.
- Changes in lifting condensation level (LCL) and level of free convection (LFC) are the critical factors driving changes in convective precipitation.
- The lowered LCL and LFC are controlled by the low-level moisture, not by air temperature.
- A large ensemble regional climate model run driven by various earth system models show similar future changes in summer convective precipitation.

Abstract

To understand the future summer precipitation changes over the Great Lakes Region (GLR), we perform an ensemble of regional climate simulations through the Pseudo-Global Warming (PGW) approach. We found that different types of convective precipitation respond to the PGW signal differently. Isolated deep convection (IDC), which is usually concentrated in the southern domain, shows an increase in precipitation to the north of the GLR. Mesoscale convective systems (MCSs), which are usually concentrated upstream of the GLR, shows a shift to the downstream region with increased precipitation. Thermodynamic variables such as convective available potential energy (CAPE) and convective inhibition energy (CIN) are found to be increased in almost the entire studied domain, providing a potential environment more (less) favorable for stronger (weaker) convection systems. Meanwhile, changes in lifting condensation level (LCL) and level of free convection (LFC) show a strong correlation with variations in convective precipitation, underscoring the significance of these thermodynamic factors in controlling precipitation over the domain. Results show that decreased LCL and LCF over places where convective precipitation is increased, is mainly contributed by the atmospheric moisture increase. In response to the prescribed warming perturbation, MCSs show more frequent occurrences downstream, while localized IDCs show more intense rain rate, longer duration, and larger rainfall area.

Plain Language Summary

To understand how summer rainfall might change in the Great Lakes Region in a warmer future climate, several climate simulations are performed using the Pseudo-Global Warming approach. We found that different types of heavy rain events react differently to the warming signal. Smaller convective rain events are found to increase mainly over the northern domain, whereas the larger and sustained rain events are found to increase over the eastern domain. The increase in rainfall is found to be associated with low-level atmospheric moisture amount, which controls the atmospheric stability. With more moisture, the atmosphere is more unstable and therefore causes more rain. The lakes play an important role in providing moisture to its downwind regions.

1 Introduction

The Laurentian Great Lakes together form the largest freshwater lake system in the world and have a significant influence on the local and regional hydroclimate (Bates et al. 1993; Scott and Huff, 1996; Li et al. 2010; Wang et al. 2022). The Great Lakes provide vast amount of evaporation which facilitate the precipitation over and surrounding the lakes. Based on three different reanalyses, Yang et al. (2023a) estimated that the local recycled moisture from the Great Lakes Region (GLR) contributes to about 35% of its precipitation. The overall precipitation plays a paramount role in regulating water levels of the Great Lakes, thereby exerting significant impact on socioeconomic activities and ecosystem services (Gronewold et al. 2013; Gronewold and Stow 2014; Kayastha et al. 2022). Several attempts have been made to understand precipitation climatology over the GLR, including the moisture sources of precipitation (Yang et al. 2023a), changes in historical precipitation characteristics (e.g., size and intensity), and the projected changes in extreme precipitation under global warming (e.g.,

d'Orgeville et al. 2014; Zobel et al. 2018; Byun et al. 2022; Cherkauer and Sinha, 2010; Mishra and Cherkauer, 2011; Michalak et al., 2013; Basile et al. 2017, among others). These analyses have vastly advanced the general understanding of precipitation over the GLR, and have also shed lights on the risk assessment for hydrometeorological extremes (e.g., drought and flooding) and their implications for the regional water-energy-food nexus in a warmer climate (Tidwell et al. 2015).

However, there are still large uncertainties in understanding the precipitation change in a warmer climate. Some major sources of these uncertainties include - limitations of both regional and global climate models for realistically capturing the hydrodynamics of the Great Lakes and their interactions with atmosphere (Sharma et al. 2018; Xue et al. 2017; 2022); poor constraints on the precipitation-related physical processes across the climate models (Notaro et al. 2021); uncertainties in projected future climate scenarios for the region; and biases arising from nonlinearities of hydrodynamic processes that are poorly described in the numerical climate models. For example, large uncertainties still exist in representing large lakes in the climate models, which limit the predictive skills in simulating precipitation near the lakes. In particular, global climate models (GCM) still lack realistic representations of lakes, partly due to the coarse resolution (Briley et al. 2021). In fact, most state-of-the-art Coupled Model Intercomparison Project (CMIP) models (version 5 and 6) either do not represent the Great Lakes or have major inconsistencies in how the lakes are simulated in terms of spatial representation and treatment of lake processes (Briley et al. 2021; Minallah and Steiner 2021; Notaro et al. 2022).

Under future warming scenarios, higher air temperature increases the water holding capacity and usually leads to increased atmospheric water vapor. Therefore, future storms might be more intense and longer lasting (Trenberth et al. 2003; Sheffield and Wood 2008; Del Genio and Kovari 2002; Pall et al. 2007; O'Gorman and Schneider 2009; Kendon et al. 2012; Prein et al. 2016; Rasmussen et al. 2020). Future mean precipitation is expected to increase with warming (Trenberth et al. 2011), with regional historical heavy precipitation reported to exceed the upper thermodynamic limit predicted by the CC relation. For example, extreme precipitation changes have been found to lie between 7 and 10% per degree of surface warming over the Great Lakes (d'Orgeville et al. 2014) and 11-14% for western Europe (Lenderink and van Meijgaard 2010).

To understand future changes in precipitation, a few studies attempted to unveil the underlying physical mechanism. Most studies used convective available potential energy (CAPE) and convective inhibition (CIN) to quantify atmospheric stability and found both CAPE and CIN to increase in a warming climate, which could affect the precipitation frequency and intensity (Gensini and Mote, 2015; Mahoney et al. 2013; Rasmussen et al. 2020; Diffenbaugh et al. 2013). Over the United States, robust increases in CAPE and CIN have been reported by Diffenbaugh et al. (2013) and Seely and Romps (2015). In particular, the increase in CIN acts as a balancing force to suppress weak to moderate convection and provides an environment where CAPE can build to extreme levels that may result in more severe convection (Rasmussen et al. 2020). Rasmussen et al. (2020) also revealed the indispensable role of temperature on thermodynamic environments. Similarly, Chen et al. (2020) demonstrated that low-CAPE and low-CIN conditions are projected to decrease in a warmer climate, resulting in decrease in light to moderate precipitation events. Frequency of heavy precipitation events are projected to increase, primarily attributed to their increased probability under given CAPE and CIN. To better

understand how CAPE and CIN change in a warmer climate, Chen et al. (2019) found that the CAPE increase is mainly due to the moister low-level atmosphere, which leads to more latent heat and buoyancy and can lift a parcel above the level of free convection more easily. On the other hand, the enhanced CIN over land is mainly a result of reduced low-level relative humidity (RH). Meanwhile, Chen et al. (2019) also identified that over oceans, the RH is slightly increased, leading to slight weakening of CIN. Such opposite response of CIN to future warming between land and water body makes it interesting to understand how climate change would affect precipitation over the Great Lakes Region, a region comprising of both land and water bodies.

Although changes in the overall precipitation and its extremes under future warming have been studied in the past, little is known about how different precipitation types change in the future. Historically, rainfall produced by mesoscale convective systems (MCSs) and non-MCS, including the isolated deep convections (IDCs), has vastly different characteristics (Li et al. 2021). By definition, MCSs are much larger in spatial coverage and longer in lifetime compared with IDCs, although their rainfall rates are similar. Therefore, the hydrologic response of MCSs and non-MCSs could be very different (Hu et al. 2020). For example, there might be a larger portion of MCS precipitation that ended as surface and subsurface runoff; while the IDC precipitation may contribute more to the evapotranspiration. Over the GLR in particular, different convection types would lead to different partition into runoff or evaporation, potentially resulting in different water levels even with the same total precipitation amount. Moreover, the MCS are mostly over the upstream, while the IDC are over the downstream based on historic observations (Wang et al. 2022). With future warming and moisture increase over entire GLR, such spatial pattern of MCS and IDC may also change.

While the previous studies investigated future precipitation changes over the GLR, there are several limitations. (1) Most of the dynamical downscaling studies directly use GCMs as boundary forcing, which may have issues properly representing lakes since lakes are not well resolved in GCMs, as discussed earlier; (2) coarse model resolution inevitably requires the use of convection parameterization, which likely hampers the accurate representation of precipitation; (3) previous studies using the Pseudo-Global Warming (PGW, Schär et al. 1996) approach usually adopt an ensemble mean of multiple Earth system models (ESMs), which prevents the possibility of uncertainty quantification; (4) besides CAPE/CIN, other thermodynamic variables such as lifting condensation level (LCL; m) and level of free convection (LFC; m) are seldomly discussed in future climate conditions; (5) how precipitation associated with different convection types will change in the future has rarely been discussed. Motivated by the previous studies focusing on future precipitation changes, the main objective of this study is to understand the physical mechanisms that lead to the respective changes in MCSs and IDCs by examining the thermodynamic environment described by CAPE, CIN, LCL and LFC. We use high-resolution convection permitting simulations and the PGW approach to study the changes by the end of this century. Using simulations with initial and boundary forcing derived from the Coupled Model Intercomparison Project Phase 6 (CMIP6) models that provide the necessary variables, we conducted a 12-member ensemble run that allows us to quantify the uncertainties in future summer precipitation due to different forcing data with regional climate simulations. This study contributes to a greater physical understanding of the future changes of different convection types over the GLR in a warmer climate.

2 Materials and Methods

2.1 Pseudo-Global Warming approach

Given the potential model errors in physics parameterizations representing the complex weather and earth system, model precipitation can differ considerably from that in observations. Thus, hydrological and agricultural impact assessments cannot directly use scenarios of future precipitation from even high-resolution models (e.g., Ines and Hansen 2006; Baigorria et al. 2007; Teutschbein and Seibert 2012; Muerth et al. 2013). The two primary current approaches to address these biases are bias-correcting model output based on observations (of means or marginal distributions) (e.g., Ines and Hansen 2006; Christensen et al. 2008; Piani et al. 2010; Teutschbein and Seibert 2012) and "delta" methods that adjust observations by model projected changes (in means or marginal distributions) (e.g., Hay et al. 2000; Räisänen and Räty 2013; Räty et al. 2014). PGW approach is an extension of the delta method and has been widely used as an alternative regional climate modeling strategy (e.g., Schär et al. 1996; Sato et al. 2007; Hara et al. 2008; Lynn et al. 2009; Rasmussen et al. 2011; Ito et al. 2016; Hoogewind et al. 2017; Gutmann et al. 2018; Adachi and Tomita, 2020; Trapp et al. 2021; Brogli et al. 2023; among others). In other words, rather than asking what will happen (as in the traditional, scenario-driven approach), PGW approach allows us to ask about the effects of particular interventions—e.g. different climate forcing scenarios—across a range of plausible futures. This idea also falls in the concept of storyline approach concept by Shepherd (2018). By asking the question this way, one can avoid the possibly low confidence in the traditional scenario-driven future projection approach. We use the PGW approach to construct the initial and boundary conditions for future scenarios. Two sets of simulations were performed, the first set is baseline simulation, representing the historical period (see description in section 2.1.2). The second set is future simulations, driven by climate forcing derived from imposing changes in the ESMs. In a simple form, the PGW can be expressed as

$$\text{Future forcing} = \text{Baseline forcing} + \Delta\text{CMIP6}_{\text{ssp585}} \quad (1)$$

where *Future forcing* represents the boundary conditions of the future climate and $\Delta\text{CMIP6}_{\text{ssp585}}$ is the future changes derived from the CMIP6 ESMs and can be expressed as

$$\Delta\text{CMIP6}_{\text{ssp585}} = \text{VAR}_{2071\text{-}2100} - \text{VAR}_{1981\text{-}2010} \quad (2)$$

Where $\text{VAR}_{2071\text{-}2100}$ represents the selected variables in the future time slice of a climate projection, and $\text{VAR}_{1981\text{-}2010}$ represents variables in the historical time slice. These variables include two-dimensional near-surface air temperature, skin temperature, sea-level pressure, surface pressure and three-dimensional air temperature, specific humidity and geopotential height at 38 pressure levels, and are necessary to drive the regional climate model, see description in section 2.1.2. SSP585 represents shared socioeconomic pathway 5 (SSP5), with an additional radiative forcing of 8.5 W/m² by the year 2100. The SSP5 is a scenario where global markets are increasingly integrated, leading to innovations and technological progress. The social and economic development, however, is based on an intensified exploitation of fossil fuel resources with a high percentage of coal and an energy-intensive lifestyle worldwide (Riahi et al. 2017).

2.1.1 Earth system model (ESM) ensemble

We chose 11 ESMs from the CMIP6 to construct the historical (1981-2010) and future (2071-2100) under the SSP585 scenario based on data availability (Table 1). They include all the

variables needed to drive the regional climate model at monthly interval. To reduce the effect of interannual variability, we used 30-year averages for each month, with temporal interpolation applied between two consecutive months to avoid abrupt variabilities of the selected variables. The changes of zonal and meridional winds in the ESMs are not considered in the PGW approach, rather they are calculated in the regional climate model corresponding to the thermal-dynamic changes. Among these 11 ESMs, we found all ESMs project increase in both air temperature and specific humidity under global warming. E3SM-1-1 projects the largest warming (9.9 °K), followed by MPI; and FGOALS projects the smallest warming (4.8 °K), followed by CanESM5. Lake surface temperature is an important lower boundary condition when running the regional climate model for a season-long simulation (Wang et al. 2022). While the lakes may not be realistically represented, their changes are the only available data source that we can use. However, we do find that EC-Earth3 shows a much stronger and unreasonable lake surface warming than the surrounding land compared with observations and fully coupled atmosphere and 3-D lake models (Xue et al. 2020). Therefore EC-Earth3 is excluded from our experiment.

Table 1. Information of the selected 11 CMIP6 models.

CMIP6* Model	abbreviation	Model full name (Reference)
ACCESS-CM2[1]	ACCESS	The Australian Community Climate and Earth System Simulator coupled model, version 2 (Bi et al., 2020)
CESM2-WACCM	CESM	The Community Earth System Model version 2 coupled with the Whole Atmosphere Community Climate Model, Version 6 (Danabasoglu et al., 2020)
CMCC-CM2-SR5	CMCC	The Euro-Mediterranean Centre on Climate Change (CMCC) coupled climate model with standard configuration (Cherchi et al., 2019)
CanESM5	CanESM5	The Canadian Earth System Model, version 5 (Swart et al., 2019)
E3SM-1-1	E3SM	The U.S. Department of Energy (DOE) new Energy Exascale Earth System Model, version 1.1 (Golaz et al., 2019)
FGOALS-f3-L	FGOALS	The Chinese Academy of Sciences (CAS) Flexible Global Ocean-Atmosphere-Land System (He et al., 2019)
GFDL-CM4	GFDL	The Geophysical Fluid Dynamics Laboratory's atmosphere-ocean coupled climate model, version 4 (Held et al., 2019)
IPSL-CM6A-LR	IPSL	The Institut Pierre-Simon Laplace (IPSL) climate model, version 6A with low resolution (Boucher et al., 2020)
MIROC6	MIROC	The Model for Interdisciplinary Research on Climate, version 6 (Tatebe et al., 2019)
MPI-ESM1-2-LR	MPI	The Max Planck Institute for Meteorology Earth System Model, version 1.2 with low resolution (Mauritsen et al., 2019)
NorESM2-LM	Nor	The coupled Norwegian Earth System Model, version 2 with low-resolution atmosphere–land and medium-resolution ocean–sea ice (Seland et al., 2020)

[*]We only use the "r1i1p1f1" variant of each selected CMIP6 model.

2.1.2 Regional Climate Model (RCM) Setup

Our RCM is the Weather and Research Forecasting (WRF) model version 4.2.2 with the Advanced Research WRF dynamic core (Skamarock et al, 2008). The model domain is centered at 45.5°N and 85.0°W and has 544 × 485 grid points in the west–east and south–north directions covering the GLR, with a grid spacing of 4 km (Figure 1). There are 50 stretched vertical levels topped at 50 hPa. The WRF model incorporates Thompson microphysics (Thompson et al., 2004, 2008), the Rapid Radiative Transfer Model for GCMs longwave and shortwave schemes (Iacono et al., 2008), and Unified Noah land surface model by Chen and Dudhia (2001). Mellor–Yamada–Janjic (MYJ) (Janjic, 1990, 1994) planetary boundary layer (PBL) scheme and Monin-Obukhov surface layer scheme are also used and coupled with an updated multilayer building environment parameterization model and a multilayer building energy model (BEP_BEM, Salamanca et al. 2009; 2010). While the use of urban models coupled to climate models requires higher computational costs, Wang et al. (2023) found that such coupled modeling can better captures urban locations' diurnal pattern of surface air temperature, skin temperature and relative humidity. No sub-grid cloud cover or shallow cumulus parameterizations are used. No boundary nudging is applied, so that the model can develop its own variability (e.g., spatial and internal variability) across the region. For the baseline, the initial and boundary conditions are constructed from 3-hourly 0.25° European Centre for Medium-Range Weather Forecasts atmospheric reanalysis of the global climate, version 5 (ERA5; Hersbach et al., 2020). The lower boundary conditions for the lake, which is the lake surface temperature is constructed from National Oceanic and Atmospheric Administration (NOAA) Great Lakes Surface Environmental Analysis (GLSEA) data set (Schwab et al., 1992) at a spatial resolution of 1.3 km. This setup was found by Wang et al. (2022) to be able to produce better air temperature and heat flux compared with observations. The simulations started on 0000 UTC on 12 May 2018 and ended on 0000 UTC 1 September 2018 for both baseline and PGW scenarios. The resulting simulations were all analyzed starting 1 June 2018. For the future scenarios, long-term (30-yr) monthly mean changes (1981-2010 versus 2071-2100) are first spatiotemporally interpolated onto the WRF grid; and then added to the baseline files (built from ERA5) during the WRF pre-processing. Then a new set of WRF simulations forced by the constructed initial and boundary conditions is conducted to represent the future scenario. When the monthly changes derived from ESMs are used for driving the WRF simulations, they need to be interpolated from monthly scale (including nearby months) to 6 hourly scale, because we update the boundary conditions for WRF every 6 hours. While there is only one summer (2018) for the baseline, the PGW signal is derived from a 30yr average and from 11 ESMs. We have conducted in total 12 WRF PGW ensemble runs, with 11 of them driven by the newly constructed initial and boundary conditions from each of the ESMs, and one driven by the ensemble mean of all these 11 ESMs. These 12 WRF ensemble runs allow us to study (1) the robustness of the future changes in different types of precipitation and the uncertainties caused by the various ESM forcing; (2) the difference between two sets of datasets: one is the WRF run driven by ESM ensemble mean (hereafter PGW_GCMavg; and this is a typical practice given limited computational resource available), and the other is ensemble mean of all 11 individual WRF runs (PGW_RCMavg; this requires much more computing resources but allows us to examine the uncertainties).

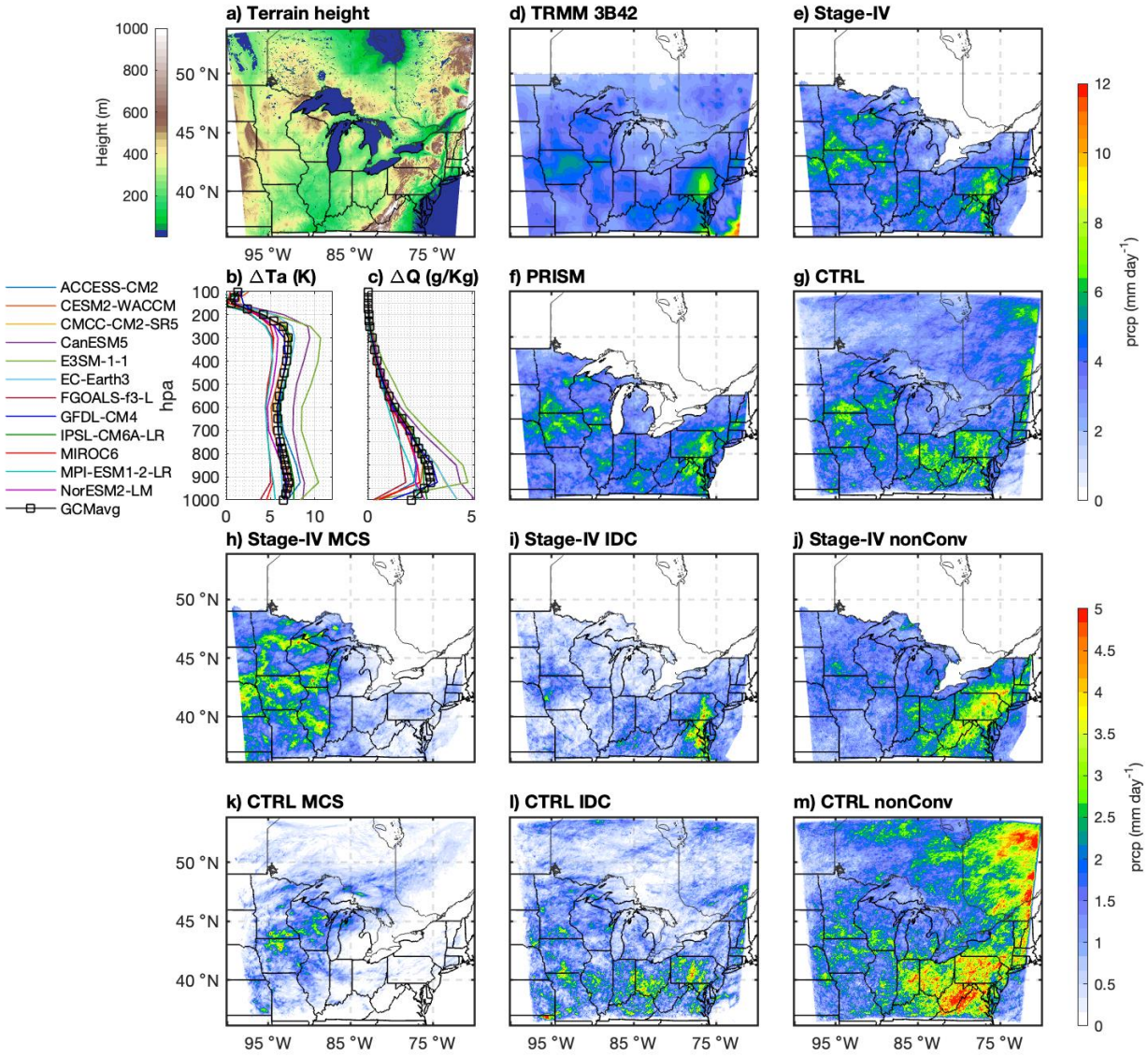

Figure 1: WRF domain setup and the simulated precipitation against reference datasets. a) WRF model domain with 2172 km × 1936 km on the west-east and south-north directions. b-c) Domain averaged seasonal mean difference in temperature (Ta) and specific humidity (Q) between future (2071-2100) and historical (1981-2010) period in each of the selected ESMs. d-g) Evaluation of the simulated precipitation against reference precipitation datasets. JJA precipitation from d) TRMM, e) Stage IV and f) PRISM, g) simulated precipitation from the baseline simulation (CTRL). h-m) Evaluation of the different precipitation types against reference precipitation datasets.

2.2 Precipitation Decomposition

As introduced in Section 1, different convective systems show clearly different temporal and geospatial patterns over the GLR as well as the central and eastern continental United States (Li et al. 2021). While both MCS and IDC rainfall amount nearly doubled during the spring and

summer (~100 mm) compared to the autumn and winter (~56 mm), MCS occurs earlier and over upstream of GLRs, and IDC occurs later and over downstream of GLRs (Wang et al. 2022). Therefore, it is important to distinguish the different types of these storms over GLR. We applied the Flexible Object Tracker (FLEXTRKR) algorithm, developed by Feng et al. (2018; 2019) and enhanced by Li et al. (2021). Compared with other tracking algorithms (e.g., Workoff et al., 2012; Prein et al., 2020), which only examine the horizontal dimensions, FLEXTRKR identifies the three-dimensional structure of convective systems and can distinguish different convective systems such as the MCS and IDC. By tracking the MCS and IDC in the baseline simulation and future projections, we analyze how the MCS and IDC characteristics, including intensity, life length, initiation location, number of events, rainfall area and total rainfall amount would change under the PGW scenarios.

2.3 Thermodynamic environment

In this study, thermodynamic variables, including CAPE, CIN, LCL and LFC are derived from the WRF output. Here we use the most unstable convective available potential energy which is a measure of instability in the troposphere that represents the total amount of potential energy available to air parcel with the maximum equivalent potential temperature within the atmosphere. To find the CAPE, air parcels from various pressure surfaces within the lowest 300 hPa in the atmosphere are released and the trajectory of a parcel that produces the maximum amount of CAPE has the most unstable CAPE. A parcel is defined as a 500-m deep parcel, with actual temperature and moisture averaged over that depth. For simplicity, we refer MUCAPE to CAPE hereafter unless otherwise noted. CIN is defined as the accumulated negative buoyant energy from the parcel starting point to the LFC. It is the amount of energy inhibiting convection and can help determine whether an environment is conducive or unfavorable for promoting convection development. In fact, as demonstrated in Rasmussen et al. (2020), CIN and CAPE are important indicators for convections. For example, environment with low CIN and high CAPE likely promotes convections but with limited strength. Environments with moderate CIN would allow CAPE to build up to higher levels; and with proper lifting mechanism, explosive convection can occur. However, if CIN is too large, then the inhibition or negative buoyant is too strong for convection to break through, so convection is suppressed (Rasmussen et al. 2020). LCL is the level at which a parcel becomes saturated and is a good estimation of cloud base height. LFC is the level at which a lifted parcel begins a free acceleration upward to the equilibrium level due to positive buoyancy. Similar to CAPE and CIN, LCL and LFC are calculated based on the parcel with maximum equivalent potential temperature within the lowest 300 hPa of the atmosphere.

2.4 Reference datasets

Three precipitation reference datasets are chosen to better validate the model performance and understand the potential discrepancy across different data products. The reference datasets are based on various data sources, including in-situ measurement and remote sensing such as radar and satellite detection. The selection of the reference data is also driven by their availability and accuracy over the Great Lakes. Details of these datasets are described as follows.

2.4.1 Parameter-Elevation Relationships on Independent Slopes Model (PRISM)

PRISM compiles climate data from various monitoring networks with rigorous quality control, and serves as the official U.S. Department of Agriculture spatial climate dataset. PRISM precipitation is available at 4-km resolution at daily time scale, factoring in terrain elements like location, elevation, coastal proximity, topographic facet orientation, vertical atmospheric layer, topographic position, and orographic effectiveness (Daly et al., 2008). PRISM data is only available over continental United States and not available over the lakes.

2.4.2 Stage IV Precipitation

Stage IV precipitation, based on radar and gauge data, is a near-real-time product processed by the Next Generation Weather Radar precipitation system and the National Weather Service River Forecast Center (RFC) precipitation processing system (Fulton et al., 1998; Seo & Breidenbach, 2002). The precipitation data is mosaicked data from the 12 RFCs, compiled by the National Center for Environmental Prediction (NCEP), providing gridded precipitation estimates at 4 km with 1-hourly and 6-hourly intervals (Nelson et al., 2016). Nelson et al. (2016) confirmed its good performance for medium to heavy precipitation. The Stage IV precipitation suffers discontinuity issues due to varied processing algorithms at different RFCs, especially in the western US. Stage IV precipitation is available over both land and the lakes.

2.4.3 TRMM

The Tropical Rainfall Measuring Mission (TRMM) is a joint mission between National Aeronautics and Space Administration (NASA) and the Japan Aerospace Exploration Agency (JAXA) designed to monitor and study tropical rainfall (Huffman et al., 2007). Utilizing the 3B42 algorithm, it generates rain gauge-adjusted multi-satellite precipitation rates and root-mean-square precipitation-error estimates. The TRMM 3B42 dataset offers 3-hourly precipitation data with a spatial resolution of 0.25°, covering the region between 50°S and 50°N since March 2000.

3 Results

3.1 Evaluation of precipitation

Precipitation simulated by WRF for the baseline (summer of 2018) is first evaluated against the reference datasets to ensure the WRF model performance is reasonable for studying the future precipitation changes. Figure 1 (d-g) shows the comparison between TRMM, PRISM, Stage-IV, as well as WRF simulated total precipitation amount from June, July and August (JJA) of 2018. First of all, all 3 observational data sources show similar geospatial pattern of precipitation over land, with larger precipitation of about 7 mm day^{-1} over Iowa at the upstream of the lakes and even larger precipitation amount at the southeast downstream of the lakes in Pennsylvania, Delaware. Although there is slight precipitation overestimation in Indiana and Ohio, the WRF model driven by ERA5 can decently capture such overall dipole pattern in precipitation, including that over the Canadian side.

When divided into different convection types, the MCS precipitation is mainly located upstream to the west of the lakes (Figure 1h), whereas IDC precipitation is mainly distributed over the southwest of the domain in the reference dataset (Figure 1i). Similarly, the non-convection

361 precipitation is also located over the southwest domain but with slightly larger magnitude
362 (Figure 1j). The simulated precipitation associated with different convections can generally
363 resemble that of the reference dataset (Figure 1k-1m), although the MCS precipitation is slightly
364 underestimated compared to the reference datasets (Figure 1k). Similar to the reference, the
365 simulated IDC precipitation is also mainly located in the southeast of the domain but with slight
366 overestimation over the south and southwest (Figure 1l). The non-convection is again well-
367 captured by the baseline simulation (Figure 1m). Overall, the baseline simulation is reasonable
368 for further investigation of future precipitation changes using this modeling configuration.
369

370 3.2 Future precipitation changes

371 3.2.1 Overall precipitation changes

372 Precipitation in future scenarios and their changes compared with baseline are shown in Figure 2.
373 Overall, the future summer precipitation shows clearly different spatial patterns with decreased
374 precipitation upstream of the Great Lakes Basin and increase over the northeast and southeast of
375 the domain (Figure 2a-b and 2d-e). Downscaled simulations with forcing derived from individual
376 GCM generally agree with the overall pattern, though with slightly different magnitudes. For
377 example, simulation driven by CanESM5, CMCC and FGOALS show the least, moderate and
378 largest amount of precipitation increase (Figure 2g-i). It is also noteworthy that the spatial
379 distribution of summer mean precipitation is very similar between PGW_GCMavg and
380 PGW_RCMavg, although PGW_RCMavg shows a smoother spatial pattern because it averages
381 across the 11 WRF simulations driven by individual ESMs. In fact, when we look at individual
382 rainstorm events, PGW_GCMavg can still capture some rainfall peaks that are forced by
383 individual ESM forcing. This indicates that, with limited computing resources, it can be
384 reasonable to conduct the WRF simulations with the ESM ensemble mean. However, to quantify
385 the uncertainty due to different forcings, it is still needed to run WRF simulations driven by
386 individual ESMs, as we do in this study. For instance, the standard deviation of precipitation
387 suggests that there might be larger uncertainties in the simulated precipitation over northeast
388 Wisconsin, south Michigan (Figure 2c). Nevertheless, the summer averaged precipitation
389 changes produced by PGW_GCMavg and PGW_RCMavg are very similar in spatial patterns
390 (Figure 2f).
391

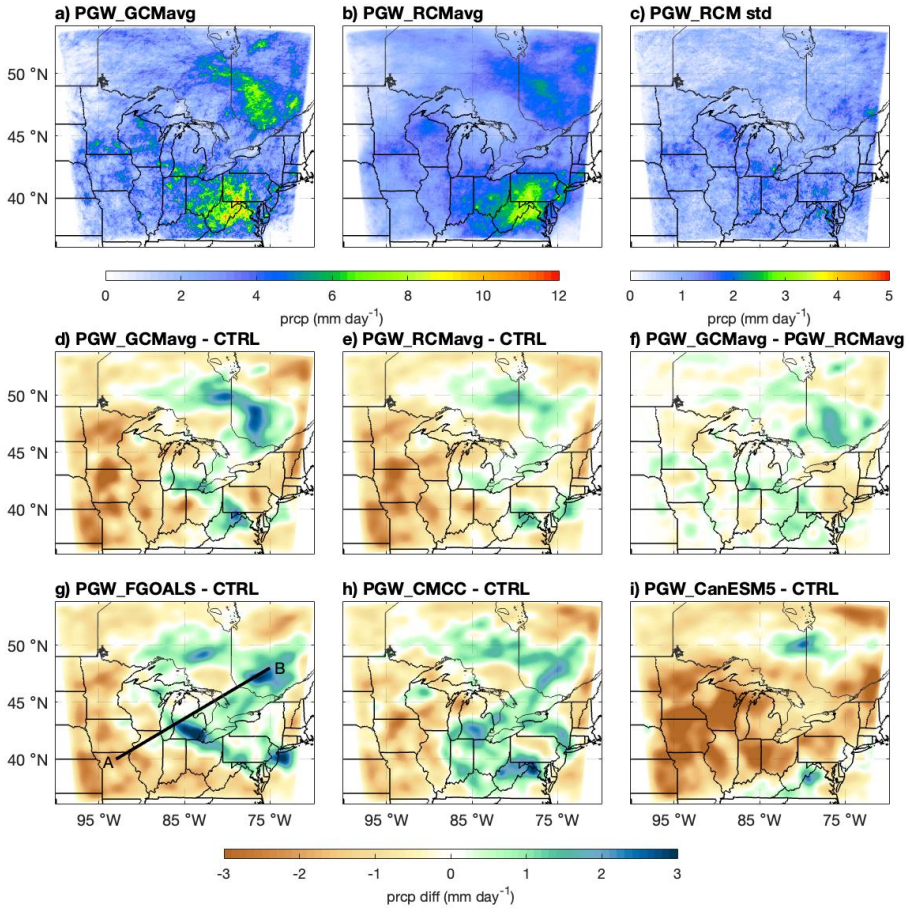

Figure 2. Simulated precipitation in future warmer climate and its changes against the baseline simulation. a-b) Simulated precipitation from PGW_GCMavg and PGW_RCMavg, c) standard deviation from the ensemble of 11 ESMs, d-e) precipitation difference between PGW_GCMavg, PGW_RCMavg and baseline, f) the difference between PGW_GCMavg and PGW_RCMavg (PGW_GCMavg minus PGW_RCMavg), g-i) difference between the selected coolest (FGOALS), moderate (CMCC), and warmest (CanESM5) ESM and the baseline simulation. The black line represents the cross-section shown in Figure 4.

3.2.2 Changes in MCSs and IDCs and their Characteristics

This section examines the future changes associated with different convection types, i.e., the MCSs and IDCs. Figure 3 displays the distribution of MCS precipitation in warmer climate (Figure 3a-b) and the changes in future projected by PGW_GCMavg and PGW_RCMavg (Figure 3c-d). In the historical period, MCS precipitation is distributed mainly over the west portion of the domain, and slightly extends to the northeast of the GLR (Figure 1k). In warmer climate, precipitation associated with MCSs seems to shift to the east with increase mainly over the southeast and east side of the domain, resulting in a decrease over its original location (Figure 3a-d) and an increase over downstream of GLR. Such spatial shift is clear and consistent in all WRF ensemble runs (not shown).

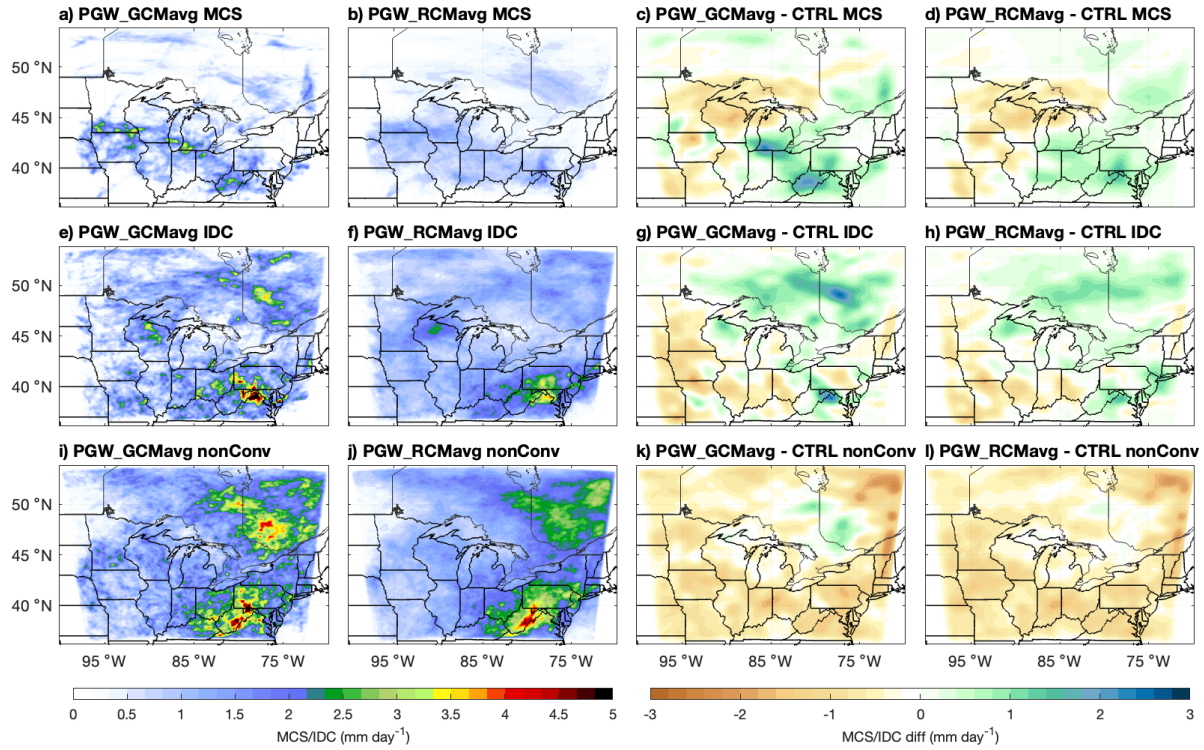

Figure 3. Spatial distribution of the different precipitation types and their changes from the baseline simulation. (a-b) Simulated MCS precipitation in a) PGW_GCMavg and b) PGW_RCMavg. (c-d) difference in MCS precipitation between c) PGW_GCMavg and CTRL d) PGW_RCMavg and CTRL. (e-h) similar as (a-d) but for IDC precipitation. (j-l) similar as (a-d) but for non-convective precipitation.

Figure (3e-f) displays the distribution of IDC precipitation and the changes projected by PGW_GCMavg and PGW_RCMavg (Figure 3g-h). Historical IDC precipitation spreads over the entire domain, with larger portion to the south and southeast side of the domain (Figure 1l). In the future scenarios, the IDC precipitation shifts further to the north and northeast side of the domain (Figure 3g-h) and agrees among all individual ensemble model (not shown). The non-convection precipitation generally shows a decreasing pattern almost over the entire domain, with the exception of the northeast domain (Figure 3i-l). Notably, although variabilities exist in the spatial distribution of different convective precipitation among different ensemble members, the general pattern agrees reasonably well between PGW_GCMavg and PGW_RCMavg, again supporting the applicability of using ensemble mean of ESM deltas as forcing to downscale future scenarios.

3.2.3 Physical Mechanisms

This section aims to understand the mechanisms for the MCS and IDC precipitation changes at the specific locations as identified in the previous section. To do so, we first study the environmental conditions for overall precipitation by examining the thermodynamic variables including CAPE, CIN, LCL and LFC. This is done for the entire domain as well as after

separating it into upwind and downwind regions to specifically understand the moisture contribution of the Great Lakes. We then study these thermodynamic factors separately for MCS and IDC events, and also investigate the characteristic changes in MCS and IDC to understand the common and unique factors causing their respective future changes.

To explore the mechanisms of the overall precipitation changes, Figure 4 shows the cross-section analysis of thermodynamic environment from the upwind to the downwind of the Great Lakes. The CAPE and CIN shown here represents the amount of available potential energy or inhibition from each level to the equilibrium level, and is different from CAPE and CIN, which represent the maximum out of these levels. In the baseline simulation, the upwind region is featured with high CAPE, relatively low LCL and LFC compared to the downwind region (Figure 4a-c), and therefore more conducive for convection at the upwind regions (Figure 1g). In a warmer climate, the existence of the Great Lakes increases evaporation and acts as a moisture source for the surrounding and downwind regions (Figure 4d-f & 4g-i). As a result of the moisture increase, it causes an increase in CAPE especially at the immediate downwind of water bodies (Figure 4e & 4h). Meanwhile, LCL also shows a decrease downwind of GLR (Figure 4e & 4h). Moreover, LFC shows an even larger decrease in this downwind region (Figure 4f and 4i). Overall, the warming-induced changes in thermodynamic environment leads to a more stable environment at the upwind with higher LCL and larger CIN; and more unstable at the downwind regions with lower LCL and LFC as well as larger CAPE and ET. These changes ultimately decrease precipitation at the interior inland region at the upstream and increase precipitation at the downwind of the Great Lakes. These changes may explain why MCS decreases upstream and IDC increases downstream of the GLR.

454
455

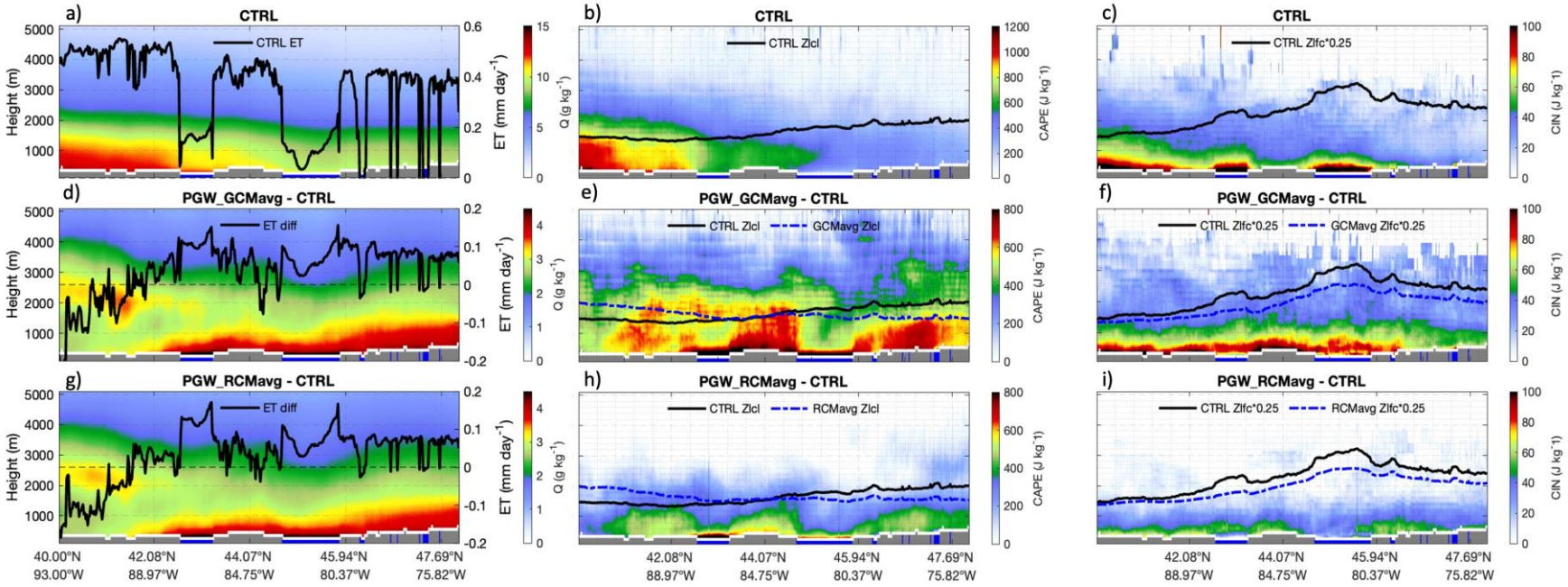

Figure 4: Cross-sectional analysis along the cross-section shown in Figure 2g, which pass over southern Lake Michigan (shown between 42.08-44.07 N) and Lake Huron (shown between 44.07- 46 N). a) Color shading indicates the specific humidity (units: g kg^{-1}), the black curve indicates the evapotranspiration along the cross-section from the land and water bodies (magnitude corresponds to y-axis on the right). d and g) color shading shows the difference in specific humidity, while the black curve indicates the difference in evapotranspiration between PGW_GCMavg, PGW_RCMavg and baseline simulation, respectively. b, e and h) are similar to a, d and g) expect that the color shading displays the CAPE, the black curve shows the height of LCL (magnitude corresponds to the left y-axis). c, f and i) are similar to b, e, h) except that the color shading shows the CIN and black curve shows the level of LFC multiplied by a factor of 0.25.

Figure 5a and 5b display regions with the same sign of changes as a result of warming for MCS and IDC precipitation among all individual ensembles. Moreover, the diurnal cycles of MCS and IDC precipitation over the identified regions are shown to pinpoint the time at which the largest differences in MCS and IDC occur. Figure 5c and 5d show that over places where MCS or IDC precipitation is increased, the largest differences occur both around local early evenings around 18 local time (LT, corresponds to 00 UTC). Alternatively, when MCS or IDC precipitation is decreased in the PGW simulations, as shown in Figure 5e and 5f, MCS precipitation decreases the most near local midnight to early morning, while IDC precipitation decreases the most near the same time. Nevertheless, we select thermodynamic environment at 18 LT to further understand the corresponding changes, both increase and decrease, in MCS and IDC precipitation. We have also looked at other timings and the general conclusions remain the same regardless of the timing selected.

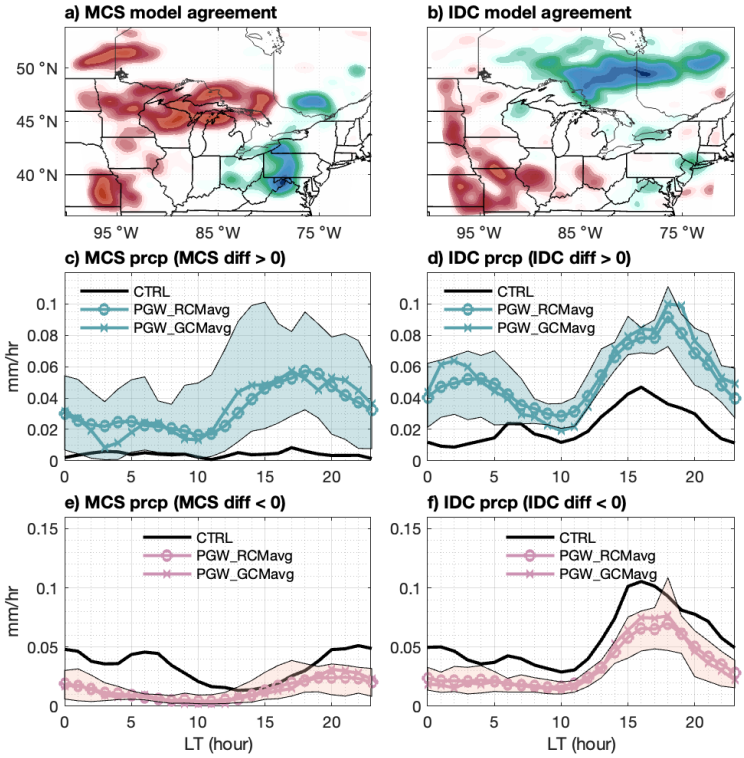

Figure 5: Identification of location and time where MCS and IDC precipitation increase and decrease due to PGW perturbation. a) Model agreement of MCS precipitation change due to the PGW perturbation, red and blue indicates MCS precipitation decrease and increase consistently among all ESM ensemble members. (c) Diurnal cycle of MCS precipitation over places where all models agree that MCS is increased in the PGW simulations (i.e., blue region in a). Black curve represents the CTRL simulation, the blue shading indicates the ensemble range, blue line with circle represents the mean of individual models (i.e., PGW_RCMavg), blue line with cross represents the simulation forced by the ESM mean as forcing (i.e., PGW_GCMavg). (e) Same as (c) except the diurnal cycle of MCS precipitation is over places where MCS is decreased (i.e., red region in a). (b, d and f) are similar as (a, c and e) but for

IDC.

To further understand the role of each of these thermodynamic factors in modulating the future precipitation changes in both MCS and IDC, Figure 6 displays the relationships between changes in CAPE and CIN as well as LCL and LFC and changes in precipitation. Surprisingly, we found that, regardless of the precipitation types (MCS or IDC) and changes (increase or decrease), CAPE and CIN always increase, suggesting that CAPE and CIN may not be the factors determining precipitation changes. In other words, regardless of precipitation increase or decrease, the negative buoyant energy air parcels need to overcome before freely ascending is universally increased. Once air parcels become positively buoyant, air parcels are more unstable with more convective potential (i.e., CAPE). The greater values of CAPE and CIN in a warmer climate have also been reported in previous studies (Rasmussen et al. 2020). Interestingly, LFC and LCL demonstrate a relatively clearer relationship between their changes and precipitation changes. Specifically, when the LCL and LFC decrease (increase), there are precipitation increase (decrease), shown in Figure 6b. This is physically intuitive because with lower LCL and LFC it is easier for air parcels to form clouds and grow into organized convection.

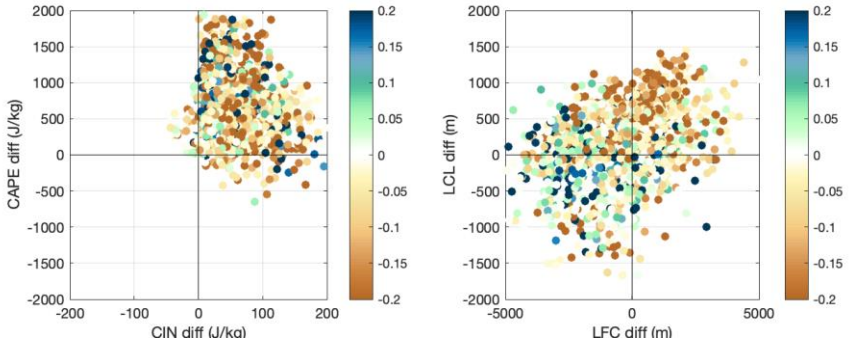

Figure 6. Scatter plots demonstrating the relationship between changes in CAPE and CIN and future precipitation change (left), as well as changes in LCL and LFC and future precipitation change (right). Color represents precipitation increase (blue) or decrease (brown) due to the PGW perturbation.

In summary, we find that there is a precipitation decrease upstream of GLR, and a precipitation increase downstream. Such changes are promoted by an environment with increased ET, CAPE, and CIN, and lower LCL and LFC over and downstream of the Great Lakes (Figure 4). However, CAPE and CIN increase is not the determining factors of the precipitation increase, instead, lower LCL and LFC are the key players increasing precipitation downstream of Great Lakes. We next examine how the warmer and moister (in terms of specific humidity) atmospheric, respectively and collectively, contribute to these changes seen in LFC and LCL.

LCL and LFC are derived as a function of vertical profiles of water vapor mixing, temperature,geopotential height, and surface pressure. These could be simplified as the equation [LFC, LCL] = *f*(water vapor mixing ratio, temperature, geopotential height, surface pressure, …). When these input values from baseline or PGW simulations are plugged into the equation, the respective LCL and LFC can be obtained. In this study, to estimate the first order effects of temperature (moisture) on LCL or LFC changes, we swap the temperature (moisture) values

from the baseline simulation with temperature (moisture) from the PGW simulations. These sensitivity calculations are designed such that no oversaturation would occur in either scenario while eliminating the need to re-run PGW simulations considering only temperature or moisture change.

Figure 7 shows the opposite effect of PGW-induced temperature and moisture on LCL and LFC changes for MCS precipitation (same for IDC; not shown). Based on Figure 6, we know that over places where precipitation is increased (decreased) both the future LCL and LFC are decreasing (increasing), which is also shown in Figure 7. However, when we only change the air temperature based on our PGW simulation output, and keep everything else the same, it leads to a higher LCL and LFC, making it more difficult for convection to occur (i.e., PGW_T; red dots). On the contrary, the future moisture changes lead to a lower LCL and LFC, which can result in more conducive environment for convection to occur (i.e., PGW_Q; yellow dots). This is because with warmer temperature, there are much higher saturated water vapor pressure following the CC relation. If specific humidity is fixed, then relative humidity will be decreased, making the vapor pressure deficit larger and more difficult to reach saturation in the lower atmosphere, resulting in higher LCL and LFC. Conversely, higher moisture amount with fixed temperature gives rise to much higher relative humidity and therefore lower LCL and LFC, and ultimately leading to more convective conducive environment.

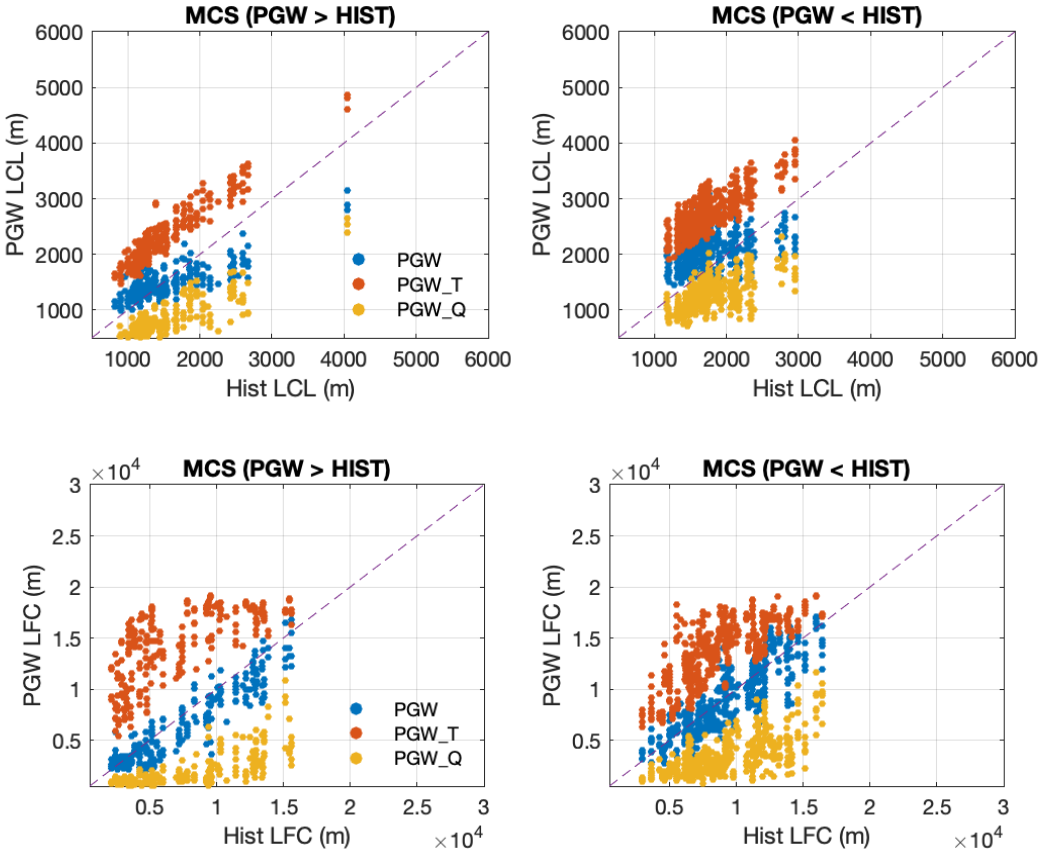

Figure 7. Scatter plots of LCL (left) and LFC (right) for baseline and perturbed calculations by changing air temperature only (indicated by orange color), and moisture only (yellow),

respectively. Left and right columns are for locations where MCS is increased and decreased in the PGW simulations (i.e., blue and red region in Figure 5a respectively). The general conclusion is the same regardless locations. The same also holds true for IDC cases and therefore not shown.

This finding highlights the importance of low-level moisture for the formation of MCS precipitation, which has been also highlighted by previous studies (e.g., Schumacher and Peters, 2017; Peters et al. 2017; Yang et al. 2023b). Schumacher and Peters (2017) found that the low-level moisture strongly regulates the amount of precipitation produced by MCSs, i.e., a 3.4% increase in vertically integrated water vapor leads to an increased by nearly 60% in the area integrated MCS precipitation. Given the importance of low-level moisture in conditioning the thermodynamic environment (Schumacher and Peters, 2017; Yang et al. 2023b), vertical profiles of RH are shown in Figure 8. For places where MCS or IDC are increased (1st and 3rd column), the RH profiles of PGW simulations are very similar to or slightly smaller than that of the baseline simulations. This is because the temperature is much warmer in PGW simulations, and the amount of moisture carried by the atmosphere is much more in the PGW simulations than the CTRL simulation. If a proper lifting mechanism exists along with the much higher CAPE (Figure 4e & 4h), both MCS and IDC precipitation would be increased in PGW simulations compared with the baseline. On the other hand, for places where MCS or IDC are decreased (2nd and 4th column), the RH profiles in PGW simulations are much drier than the baseline simulations. Such drier conditions lead to higher LFC/LCL (Figure 4, 6 & 7), making it difficult for convection to occur, which ultimately cause less precipitation associated with MCS and IDC events (Figure 3 & 5).

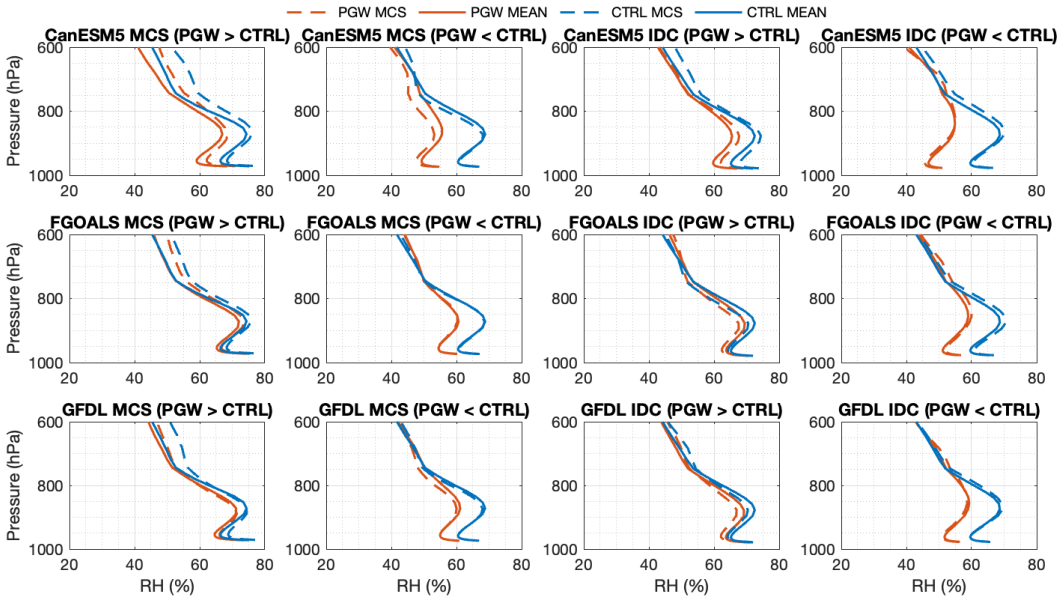

Figure 8. Relative humidity profiles over regions where MCS/IDC are increased (1st and 3rd columns) and decreased (2nd and 4th columns) for selected GCMs at 18 LT. All other GCMs show the same behavior and are not shown.

The analysis above suggests that the key thermodynamic factors that cause the precipitation

increase overall is the lower LCL and LFC; and that the increased moisture in future is the main driver of such decrease in LCL and LFC. This mechanism is true for both MCS and IDC when study the entire domain as a whole. However, from Figures 2-3, we know that the changes in MCS and IDC are spatially distinct. Here we further examine the differences between these two types of precipitation changes. To explain the differences in spatial coverage of MCS precipitation between the baseline and the PGW simulations, Figure 9 displays all the MCS tracks from initiation to dissipation for the entire season. The MCS tracks agree with the overall spatial pattern of MCS precipitation amount (Figure 1k, 3a & 3b). For example, MCS tracks gather towards the western portion of the domain with only two MCS events initiated in the south and southeast of GLR in the baseline simulation (Figure 9a). In contrast, in the PGW simulations, there are more tracks that originate over the central and southern domain and bring precipitation to the southeast of GLR (Figure 9b), which explains the increase in MCS precipitation in Ohio, Pennsylvania and West Virginia (Figure 3c-d). MCS events are less frequent near the US-Canada border in Wisconsin and Michigan (Figure 9a & 9b), resulting in MCS precipitation decrease over these regions in PGW_GCMavg (Figure 3c-d). there are also fewer MCS tracks in PGW simulations compared with the baseline simulation (e.g., 28 in PGW_GCMavg compared to 32 in CTRL).

Given their relative short life length and travel distance, IDC initiation locations are considered to be good proxies for the IDC event locations. The total number of IDCs witnesses a 40% decrease from 8887 in the baseline to 5418 in PGW_GCMavg. Such a reduction in IDC frequency is consistent with previous studies that show decrease in frequency in light to moderate precipitation (Chen et al.2019, Rasmussen et al. 2020). We also found that the reduction is almost universal in the entire domain (Figure 9c-d). Nevertheless, there are still increase in IDC precipitation amount in PGW simulations over the domain as shown in Figures 3g-h. This increase is due to more intense precipitation rate, longer duration, and large spatial coverage (Figure 9e-h). Therefore, the mechanisms for the changes in MCS and IDC precipitation in future are different. The shift of the MCS precipitation from upstream to downstream is mainly due to the changes in MCS tracks, whereas the increase of IDC precipitation can be explained by a combination of increase in precipitation intensity, duration and spatial coverage, despite the decreased frequency over entire domain.

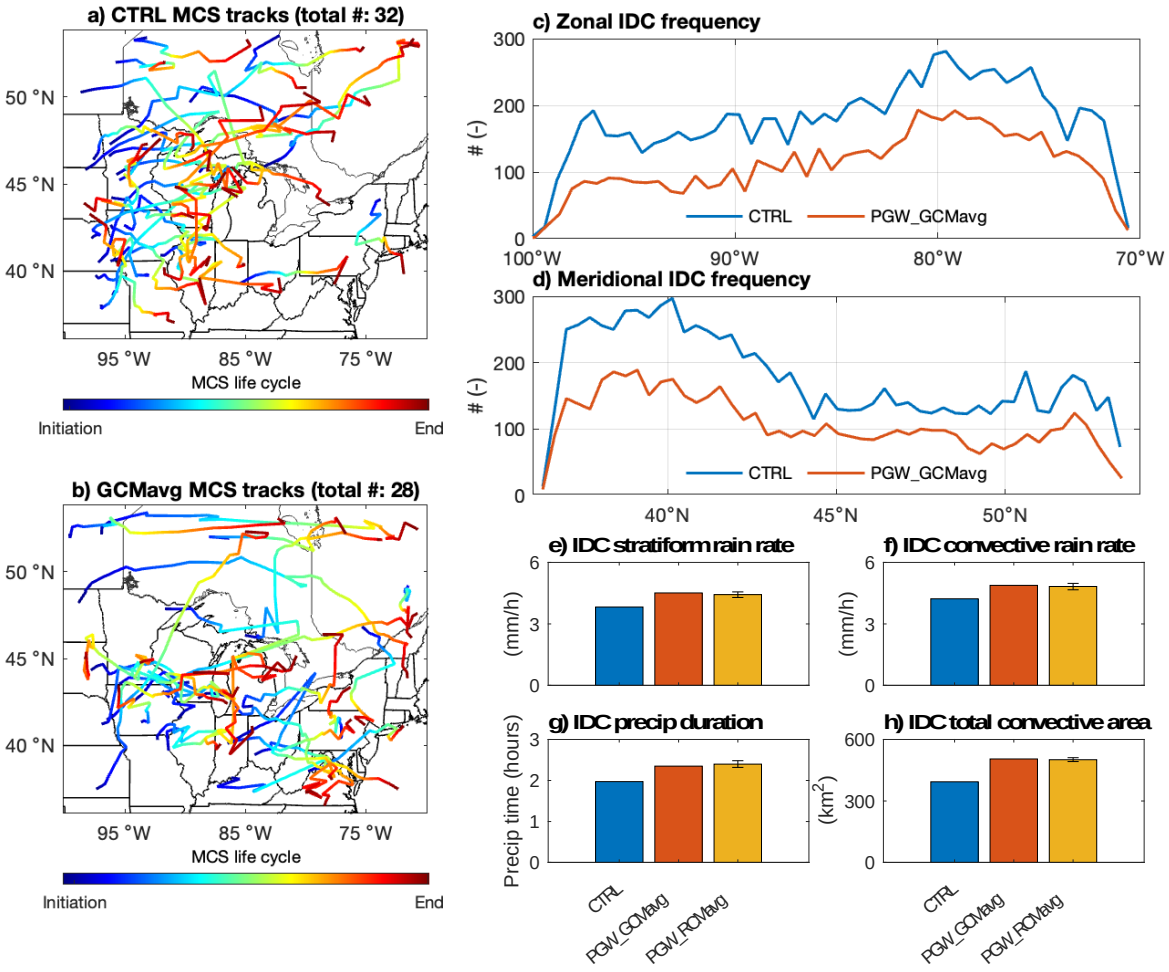

Figure 9: MCS and IDC characteristics for CTRL and PGW_GCMavg. a and b) the MCS tracks from initiation to dissipation through their entire life cycles. c and d) the zonal and meridional frequency of IDCs. e-h) IDC characteristics including stratiform rain rate, convective rain rate, duration and convective area for CTRL, PGW_GCMavg and PGW_RCMavgs, the error bars in the third columns indicate the standard deviation across different ensemble members.

4 Summary and Discussions

We performed an ensemble of regional climate simulations through the Pseudo-Global Warming (PGW) approach to understand the future summer precipitation change over the Great Lakes Region (GLR). Results show that the location of future precipitation is shifted for different convection types in the PGW simulations. More intense, long-lasting MCS induced precipitation move to the east and southeast of the GLR. Due to the shift in precipitation systems, there is a net precipitation decrease upwind and precipitation increase downwind of the Great Lakes. The variation in different convective precipitation is mainly associated with thermodynamic changes in LCL and LFC, rather than CAPE and CIN, although they are found to be increased almost over the entire domain, similar to those found in previous studies. This suggests that CAPE and

CIN are not the determining factor in controlling the changes in precipitation. Instead, LCL and LFC changes play more critical roles. Specifically, over places where LCL and LFC are lower, the amount of precipitation is likely to increase for both MCSs and IDCs in the PGW simulations. Our results further suggest that PGW induced moisture and temperature change exert the opposite effect on the LCL and LFC, i.e., PGW induced moisture increase is more likely to lower the LCL and LFC whereas PGW induced temperature increase is more likely to lift LCL and LFC.

The cross-section analysis indicates a reduction in evaporation at the upwind region, likely attributable to the concurrent precipitation decrease. As a result of the decrease in latent heat flux, more energy is partitioned into sensible heat, thus increasing the surface air temperature. The warmer and drier atmosphere at the upwind region become less favorable for convection to occur, as indicated by higher LCL. However, the existence of the Great Lakes serves as an abundant source of moisture for its surrounding and downwind region. The increase in atmospheric moisture lowers the LCL and LFC and thereby facilitating convection, especially for the downwind regions.

While many previous studies utilize the PGW approach with the ensemble mean of GCM deltas providing the future forcing, the uncertainty of ensemble members driven by individual GCMs has rarely been evaluated. In this study, we evaluated the ensemble mean of GCM forcings by running the PGW simulation derived from each individual GCM model and compared with the ensemble mean. Overall, while there exist variabilities in terms of MCS or IDC characteristics among the PGW simulations based on individual GCMs, the mean of simulations driven by each individual GCM forcings is very similar to that of the simulation driven by the mean of GCM forcings. As such, our results indicate that it would be appropriate for future analysis containing more years to adopt the ensemble mean of GCM forcings to drive regional climate models, as our results show that this approach would adequately capture the overarching signals and physical mechanism induced by perturbations.

While this study analyzes one summer in 2018, the findings are important due to the following reasons. First, 2018 was a neutral year over the Great Lakes region, and its MCS and IDC patterns are similar to the multi-year climatology, as presented in Wang et al. (2022). Second, the 12 ensemble members in the PGW simulations show consistent results in terms of the future summer precipitation changes although the magnitude varies across ESMs. While we present the ensemble mean results in the main manuscript, all analyses have been done for each ensemble member, and results are consistent between all ensemble members. This suggests that the physical mechanisms, for both the MCS and IDC precipitation changes, are consistent across all the ensemble members.

Acknowledgments

This research is based on work supported by COMPASS-GLM, a multi-institutional project supported by the U.S. Department of Energy, Office of Science, Biological and Environmental Research. This is Contribution No. xx of the Great Lakes Research Center at Michigan Tech. Computational resources are provided by the DOE-supported National Energy Research

Scientific Computing Center. The Pacific Northwest National Laboratory is operated for DOE by Battelle Memorial Institute under contract DE-AC05-76RL01830.

Open Research

The PRISM precipitation data is available online at http://prism.oregonstate.edu/recent/ (Daly et al. 2008; accessed Mar. 2023).
The CMIP6 portal is available at https://aims2.llnl.gov/search (accessed Jan. 2023).
The TRMM Data available at https://search.earthdata.nasa.gov/search?q=TRMM_3B42 (Huffman et al., 2007; accessed Jun. 2023).
The Stage IV precipitation is available at: https://data.eol.ucar.edu/cgi-bin/codiac/fgr_form/id=21.093 (Fulton et al., 1998; Seo & Breidenbach, 2002; accessed Jun. 2023).
Reference dataset for convective precipitation dataset is available at: https://portal.nersc.gov/project/m3525/jli628/MCS_IDC_dataset/v1.1/ (Li et al. 2021; accessed Aug. 2023)
Our code repository: 10.5281/zenodo.10594122, subject to change after revision.

References

Adachi, S. A., & Tomita, H. (2020). Methodology of the Constraint Condition in Dynamical Downscaling for Regional Climate Evaluation: A Review. *Journal of Geophysical Research: Atmospheres*, *125*(11). https://doi.org/10.1029/2019jd032166

Baigorria, G., Jones, J., Shin, D., Mishra, A., & O'Brien, J. (2007). Assessing uncertainties in crop model simulations using daily bias-corrected Regional Circulation Model outputs. *Climate Research*, *34*, 211–222. https://doi.org/10.3354/cr00703

Basile, S. J., Rauscher, S. A., & Steiner, A. L. (2017). Projected precipitation changes within the Great Lakes and Western Lake Erie Basin: a multi-model analysis of intensity and seasonality. *International Journal of Climatology*, 37(14), 4864–4879. https://doi.org/10.1002/joc.5128

Bates, G. T., Giorgi, F., & Hostetler, S. W. (1993). Toward the Simulation of the Effects of the Great Lakes on Regional Climate. *Monthly Weather Review*, 121(5), 1373–1387. https://doi.org/10.1175/1520-0493(1993)121<1373:ttsote>2.0.co;2

Bi, D., Dix, M., Marsland, S., O'Farrell, S., Sullivan, A., Bodman, R., et al. (2020). Configuration and spin-up of ACCESS-CM2, the new generation Australian Community Climate and Earth System Simulator Coupled Model. *Journal of Southern Hemisphere Earth Systems Science*, 70(1), 225-251. https://doi.org/10.1071/ES19040.

Boucher, O., Servonnat, J., Albright, A. L., Aumont, O., Balkanski, Y., Bastrikov, V., et al. (2020). Presentation and evaluation of the IPSL-CM6A-LR climate model. *Journal of*

Advances in Modeling Earth Systems, 12(7), e2019MS002010. https://doi.org/10.1029/2019MS002010.

Briley, L. J., R. B. Rood, and M. Notaro (2021). Large lakes in climate models: A Great Lakes case study on the usability of CMIP5. *J. Great Lakes Res.*, 47, 405–418, https://doi.org/10.1016/j.jglr.2021.01.010.

Brogli, R., Heim, C., Mensch, J., Sørland, S. L., & Schär, C. (2023). The pseudo-global-warming (PGW) approach: methodology, software package PGW4ERA5 v1.1, validation, and sensitivity analyses. *Geoscientific Model Development*, *16*(3), 907–926. https://doi.org/10.5194/gmd-16-907-2023

Bryan, A. M., Steiner, A. L., & Posselt, D. J. (2015). Regional modeling of surface-atmosphere interactions and their impact on Great Lakes hydroclimate. *Journal of Geophysical Research*, 120(3), 1044–1064. https://doi.org/10.1002/2014JD022316

Byun, K., Sharma, A., Wang, J., Tank, J. L., & Hamlet, A. F. (2022). Intercomparison of Dynamically and Statistically Downscaled Climate Change Projections over the Midwest and Great Lakes Region. *Journal of Hydrometeorology*, *23*(5), 659–679. https://doi.org/10.1175/jhm-d-20-0282.1

Chen, J., Dai, A., Zhang, Y., & Rasmussen, K. L. (2019). Changes in Convective Available Potential Energy and Convective Inhibition Under Global Warming Changes in Convective Available Potential Energy and Convective Inhibition Under Global Warming. *Journal of Climate*, *33*(6), 2025–2050. https://doi.org/10.1175/jcli-d-19-0461.1

Chen, J., Dai, A., & Zhang, Y. (2020). Linkage between Projected Precipitation and Atmospheric Thermodynamic Changes. *Journal of Climate*, *33*(16), 7155–7178. https://doi.org/10.1175/jcli-d-19-0785.1

Chen, F., & Dudhia, J. (2001). Coupling an advanced land surface-hydrology model with the Penn State-NCAR MM5 modeling system. Part I: Model implementation and sensitivity. *Monthly Weather Review*, *129*(4), 569–585. https://doi.org/10.1175/1520-0493(2001)129<0587:caalsh>2.0.co;2

Cherchi, A., Fogli, P. G., Lovato, T., Peano, D., Iovino, D., Gualdi, S., et al. (2019). Global mean climate and main patterns of variability in the CMCC-CM2 coupled model. *Journal of Advances in Modeling Earth Systems*, 11(1), 185-209. https://doi.org/10.1029/2018MS001369.

Cherkauer, K. A., & Sinha, T. (2010). Hydrologic impacts of projected future climate change in the Lake Michigan region. *Journal of Great Lakes Research*, 36(SP2), 33–50. https://doi.org/10.1016/j.jglr.2009.11.012

680 Christensen, J. H., Boberg, F., Christensen, O. B., & Lucas-Picher, P. (2008). On the need for
681 bias correction of regional climate change projections of temperature and precipitation.
682 *Geophysical Research Letters*, *35*(20). https://doi.org/10.1029/2008GL035694
683
684 Daly, C., Halbleib, M., Smith, J. I., Gibson, W. P., Doggett, M. K., Taylor, G. H., et al. (2008).
685 Physiographically sensitive mapping of climatological temperature and precipitation
686 across the conterminous United States. *International Journal of Climatology*, *28*(15),
687 2031–2064. https://doi.org/10.1002/joc.1688
688
689 Danabasoglu, G., Lamarque, J. F., Bacmeister, J., Bailey, D., DuVivier, A., Edwards, J., et al.
690 (2020). The community earth system model version 2 (CESM2). *Journal of Advances in*
691 *Modeling Earth Systems*, 12(2), e2019MS001916.
692 https://doi.org/10.1029/2019MS001916.
693
694 Del Genio, A. D., & Kovari, W. (2002). Climatic Properties of Tropical Precipitating Convection
695 under Varying Environmental Conditions. *Journal of Climate*, *15*(18), 2597–2615.
696 https://doi.org/10.1175/1520-0442(2002)015<2597:CPOTPC>2.0.CO;2
697
698 Diffenbaugh, N. S., Scherer, M., & Trapp, R. J. (2013). Robust increases in severe thunderstorm
699 environments in response to greenhouse forcing. *Proceedings of the National Academy of*
700 *Sciences*, *110*(41), 16361–16366. https://doi.org/10.1073/pnas.1307758110
701
702 d'Orgeville, M., Peltier, W. R., Erler, A. R., & Gula, J. (2014). Climate change impacts on Great
703 Lakes Basin precipitation extremes. *Journal of Geophysical Research: Atmospheres*,
704 *119*(18), 10,799-10,812. https://doi.org/10.1002/2014JD021855
705
706 Feng, Z., Leung, L. R., Jr, R. A. H., Hagos, S., Hardin, J., Yang, Q., et al. (2018). Structure and
707 Evolution of Mesoscale Convective Systems: Sensitivity to Cloud Microphysics in
708 Convection-Permitting Simulations Over the United States. *Journal of Advances in*
709 *Modeling Earth Systems*, *10*(7), 1470–1494. https://doi.org/10.1029/2018ms001305
710
711 Feng, Z., Jr, R. A. H., Leung, L. R., Song, F., Hardin, J. C., Wang, J., et al. (2019).
712 Spatiotemporal Characteristics and Large-Scale Environments of Mesoscale Convective
713 Systems East of the Rocky Mountains. *Journal of Climate*, *32*(21), 7303–7328.
714 https://doi.org/10.1175/jcli-d-19-0137.1
715
716 Fulton, R. A., Breidenbach, J. P., Seo, D.-J., Miller, D. A., & O'Bannon, T. (1998). The WSR-
717 88D Rainfall Algorithm. *Weather and Forecasting*, *13*(2), 377–395.
718 https://doi.org/10.1175/1520-0434(1998)013<0377:twra>2.0.co;2
719
720 Gensini, V. A., & Mote, T. L. (2015). Downscaled estimates of late 21st century severe weather
721 from CCSM3. *Climatic Change*, *129*(1–2), 307–321. https://doi.org/10.1007/s10584-014-
722 1320-z
723
724 Golaz, J. C., Caldwell, P. M., Van Roekel, L. P., Petersen, M. R., Tang, Q., Wolfe, J. D., et al.
725 (2019). The DOE E3SM coupled model version 1: Overview and evaluation at standard

resolution. *Journal of Advances in Modeling Earth Systems*, 11(7), 2089-2129. https://doi.org/10.1029/2018MS001603.

Gronewold, A. D., Fortin, V., Lofgren, B., Clites, A., Stow, C. A., & Quinn, F. (2013). Coasts, water levels, and climate change: A Great Lakes perspective. *Climatic Change*, 120(4), 697–711. https://doi.org/10.1007/s10584-013-0840-2

Gronewold, A. D., & Stow, C. A. (2014). Water Loss from the Great Lakes. *Science*, 343(6175), 1084–1085. https://doi.org/10.1126/science.1249978

Gutmann, E. D., Rasmussen, R. M., Liu, C., Ikeda, K., Bruyere, C. L., Done, J. M., et al. (2018). Changes in hurricanes from a 13-Yr convection-permitting pseudo- global warming simulation. *Journal of Climate*, *31*(9), 3643–3657. https://doi.org/10.1175/jcli-d-17-0391.1

Hara, M., Yoshikane, T., Kawase, H., & Kimura, F. (2008). Estimation of the Impact of Global Warming on Snow Depth in Japan by the Pseudo-Global-Warming Method. *Hydrological Research Letters*, *2*, 61–64. https://doi.org/10.3178/hrl.2.61

Hay, L. E., Wilby, R. L., & Leavesley, G. H. (2000). A comparison of delta change and downscaled GCM scenarios for three mountainous basins in the United States. *JAWRA Journal of the American Water Resources Association*, *36*(2), 387–397. https://doi.org/10.1111/j.1752-1688.2000.tb04276.x

He, B., Bao, Q., Wang, X., Zhou, L., Wu, X., Liu, Y., et al. (2019). CAS FGOALS-f3-L model datasets for CMIP6 historical atmospheric model intercomparison project simulation. *Advances in Atmospheric Sciences*, 36(8), 771-778. https://doi.org/10.1007/s00376-019-9027-8.

Held, I., Guo, H., Adcroft, A., Dunne, J., Horowitz, L., Krasting, J., et al. (2019). Structure and performance of GFDL's CM4. 0 climate model. *Journal of Advances in Modeling Earth Systems*, 11(11), 3691-3727. https://doi.org/10.1029/2019MS001829.

Hersbach, H., Bell, B., Berrisford, P., Hirahara, S., Horányi, A., Muñoz-Sabater, J., et al. (2020). The ERA5 global reanalysis. *Quarterly Journal of the Royal Meteorological Society*, *146*(730), 1999–2049. https://doi.org/10.1002/qj.3803

Hoogewind, K. A., Baldwin, M. E., & Trapp, R. J. (2017). The Impact of Climate Change on Hazardous Convective Weather in the United States: Insight from High-Resolution Dynamical Downscaling. *Journal of Climate*, *30*(24), 10081–10100. https://doi.org/10.1175/jcli-d-16-0885.1

Hu, H., Leung, L. R., & Feng, Z. (2020). Understanding the Distinct Impacts of MCS and Non-MCS Rainfall on the Surface Water Balance in the Central United States Using a Numerical Water-Tagging Technique. *Journal of Hydrometeorology*, *21*(10), 2343–2357. https://doi.org/10.1175/JHM-D-20-0081.1

Huffman, G. J., Bolvin, D. T., Nelkin, E. J., Wolff, D. B., Adler, R. F., Gu, G., et al. (2007). The TRMM Multisatellite Precipitation Analysis (TMPA): Quasi-Global, Multiyear, Combined-Sensor Precipitation Estimates at Fine Scales. *Journal of Hydrometeorology*, *8*(1), 38–55. https://doi.org/10.1175/jhm560.1

Iacono, M. J., Delamere, J. S., Mlawer, E. J., Shephard, M. W., Clough, S. A., & Collins, W. D. (2008). Radiative forcing by long-lived greenhouse gases: Calculations with the AER radiative transfer models. *Journal of Geophysical Research: Atmosphere*. https://doi.org/10.1029/2008jd009944

Ines, A. V. M., & Hansen, J. W. (2006). Bias correction of daily GCM rainfall for crop simulation studies. *Agricultural and Forest Meteorology*, *138*(1–4), 44–53. https://doi.org/10.1016/j.agrformet.2006.03.009

Ito, R., Takemi, T., & Arakawa, O. (2016). A Possible Reduction in the Severity of Typhoon Wind in the Northern Part of Japan under Global Warming: A Case Study. *SOLA*, *12*(0), 100–105. https://doi.org/10.2151/sola.2016-023

Janjić, Z. I. (1990). The Step-Mountain Coordinate: Physical Package. *Monthly Weather Review*, *118*(7), 1429–1443. https://doi.org/10.1175/1520-0493(1990)118<1429:TSMCPP>2.0.CO;2

Janjić, Z. I. (1994). The Step-Mountain Eta Coordinate Model: Further Developments of the Convection, Viscous Sublayer, and Turbulence Closure Schemes. *Monthly Weather Review*, *122*(5), 927–945. https://doi.org/10.1175/1520-0493(1994)122<0927:tsmecm>2.0.co;2

Kayastha, M. B., Ye, X., Huang, C., & Xue, P. (2022). Future rise of the Great Lakes water levels under climate change. *Journal of Hydrology*, *612*, 128205. https://doi.org/10.1016/j.jhydrol.2022.128205

Kendon, E. J., Roberts, N. M., Senior, C. A., & Roberts, M. J. (2012). Realism of Rainfall in a Very High-Resolution Regional Climate Model. *Journal of Climate*, *25*(17), 5791–5806. https://doi.org/10.1175/JCLI-D-11-00562.1

Lenderink, G., & Meijgaard, E. van. (2010). Linking increases in hourly precipitation extremes to atmospheric temperature and moisture changes. *Environmental Research Letters*, 5(2), 025208. https://doi.org/10.1088/1748-9326/5/2/025208

Li, J., Feng, Z., Qian, Y., & Leung, L. R. (2021). A high-resolution unified observational data product of mesoscale convective systems and isolated deep convection in the United States for 2004–2017. *Earth System Science Data*, *13*(2), 827–856. https://doi.org/10.5194/essd-13-827-2021

Li, X., S. Zhong, X. Bian, W. E. Heilman, Y. Luo, and W. Dong (2010), Hydroclimate and variability in the Great Lakes region as derived from the North American Regional Reanalysis, *J. Geophys. Res.*, 115, D12104, doi:10.1029/2009JD012756.

Lynn, B., Healy, R., & Druyan, L. (2009). Investigation of Hurricane Katrina characteristics for future, warmer climates. *Climate Research*, *39*(June), 75–86. https://doi.org/10.3354/cr00801

Mahoney, K., Alexander, M., Scott, J. D., & Barsugli, J. (2013). High-Resolution Downscaled Simulations of Warm-Season Extreme Precipitation Events in the Colorado Front Range under Past and Future Climates. *Journal of Climate*, *26*(21), 130705134202004. https://doi.org/10.1175/JCLI-D-12-00744.1

Mauritsen, T., Bader, J., Becker, T., Behrens, J., Bittner, M., Brokopf, R., et al. (2019). Developments in the MPI-M Earth System Model version 1.2 (MPI-ESM1. 2) and its response to increasing CO2. *Journal of Advances in Modeling Earth Systems*, 11(4), 998-1038. https://doi.org/10.1029/2018MS001400.

Michalak, A. M., Anderson, E. J., Beletsky, D., Boland, S., Bosch, N. S., Bridgeman, T. B., et al. (2013). Record-setting algal bloom in Lake Erie caused by agricultural and meteorological trends consistent with expected future conditions. *Proceedings of the National Academy of Sciences*, *110*(16), 6448–6452. https://doi.org/10.1073/pnas.1216006110

Mishra, V., & Cherkauer, K. A. (2011). Influence of cold season climate variability on lakes and wetlands in the Great Lakes region. *Journal of Geophysical Research: Atmospheres*, *116*(D12). https://doi.org/10.1029/2010JD015063

Minallah, S., & Steiner, A. L. (2021). Analysis of the Atmospheric Water Cycle for the Laurentian Great Lakes Region Using CMIP6 Models. *Journal of Climate*, *34*(12), 4693–4710. https://doi.org/10.1175/JCLI-D-20-0751.1

Muerth, M. J., St-Denis, B. G., Ricard, S., Velázquez, J. A., Schmid, J., Minville, M., et al. (2013). On the need for bias correction in regional climate scenarios to assess climate change impacts on river runoff. *Hydrology and Earth System Sciences*, *17*(3), 1189–1204. https://doi.org/10.5194/hess-17-1189-2013

Nelson, B. R., Prat, O. P., Seo, D. J., & Habib, E. (2016). Assessment and Implications of NCEP Stage IV Quantitative Precipitation Estimates for Product Intercomparisons. *Weather and Forecasting*, *31*(2), 371–394. https://doi.org/10.1175/waf-d-14-00112.1

Notaro, M., Holman, K., Zarrin, A., Fluck, E., Vavrus, S., & Bennington, V. (2013). Influence of the Laurentian Great Lakes on Regional Climate. *Journal of Climate*, *26*(3), 789–804. https://doi.org/10.1175/JCLI-D-12-00140.1

862 Notaro, M., Zhong, Y., Xue, P., Peters-Lidard, C., Cruz, C., Kemp, E., et al. (2021). Cold season
863 performance of the NU-WRF regional climate model in the Great Lakes Region. *Journal*
864 *of Hydrometeorology*, 22(9), 2423–2454. https://doi.org/10.1175/JHM-D-21-0025.1
865
866 Notaro, M., Jorns, J., & Briley, L. (2022). Representation of Lake–Atmosphere Interactions and
867 Lake-Effect Snowfall in the Laurentian Great Lakes Basin among HighResMIP Global
868 Climate Models. *Journal of the Atmospheric Sciences*, *79*(5), 1325–1347.
869 https://doi.org/10.1175/JAS-D-21-0249.1
870
871 O'Gorman, P. A., & Schneider, T. (2009). Scaling of Precipitation Extremes over a Wide Range
872 of Climates Simulated with an Idealized GCM. *Journal of Climate*, *22*(21), 5676–5685.
873 https://doi.org/10.1175/2009JCLI2701.1
874
875 Pall, P., Allen, M. R., & Stone, D. A. (2007). Testing the Clausius–Clapeyron constraint on
876 changes in extreme precipitation under CO2 warming. *Climate Dynamics*, *28*(4), 351–
877 363. https://doi.org/10.1007/s00382-006-0180-2
878
879 Peters, J. M., Nielsen, E. R., Parker, M. D., Hitchcock, S. M., & Schumacher, R. S. (2017). The
880 impact of low-level moisture errors on model forecasts of an MCS observed during
881 PECAN. *Monthly Weather Review*, *145*(9), 3599–3624. https://doi.org/10.1175/mwr-d-
882 16-0296.1
883
884 Piani, C., Haerter, J. O., & Coppola, E. (2010). Statistical bias correction for daily precipitation
885 in regional climate models over Europe. *Theoretical and Applied Climatology*, *99*(1–2),
886 187–192. https://doi.org/10.1007/s00704-009-0134-9
887
888 Prein, A. F., Rasmussen, R. M., Ikeda, K., Liu, C., Clark, M. P., & Holland, G. J. (2017). The
889 future intensification of hourly precipitation extremes. *Nature Climate Change*, *7*(1), 48–
890 52. https://doi.org/10.1038/nclimate3168
891
892 Prein, A. F., Liu, C., Ikeda, K., Bullock, R., Rasmussen, R. M., Holland, G. J., & Clark, M.
893 (2020). Simulating North American mesoscale convective systems with a convection-
894 permitting climate model. *Climate Dynamics*, *55*(1–2), 95–110.
895 https://doi.org/10.1007/s00382-017-3993-2
896
897 Räisänen, J., & Räty, O. (2013). Projections of daily mean temperature variability in the future:
898 cross-validation tests with ENSEMBLES regional climate simulations. *Climate*
899 *Dynamics*, *41*(5–6), 1553–1568. https://doi.org/10.1007/s00382-012-1515-9
900
901 Rasmussen, K. L., Prein, A. F., Rasmussen, R. M., Ikeda, K., & Liu, C. (2020). Changes in the
902 convective population and thermodynamic environments in convection-permitting
903 regional climate simulations over the United States. *Climate Dynamics*, 55(1–2), 383–
904 408. https://doi.org/10.1007/s00382-017-4000-7
905
906 Rasmussen, R., Liu, C., Ikeda, K., Gochis, D., Yates, D., Chen, F., et al. (2011). High-Resolution
907 Coupled Climate Runoff Simulations of Seasonal Snowfall over Colorado: A Process

908 Study of Current and Warmer Climate. *Journal of Climate*, *24*(12), 3015–3048.
909 https://doi.org/10.1175/2010jcli3985.1
910
911 Räty, O., Räisänen, J., & Ylhäisi, J. S. (2014). Evaluation of delta change and bias correction
912 methods for future daily precipitation: intermodel cross-validation using ENSEMBLES
913 simulations. *Climate Dynamics*, *42*(9–10), 2287–2303. https://doi.org/10.1007/s00382-
914 014-2130-8
915
916 Riahi, K., Vuuren, D. P. van, Kriegler, E., Edmonds, J., O'Neill, B. C., Fujimori, S., et al.
917 (2017). The Shared Socioeconomic Pathways and their energy, land use, and greenhouse
918 gas emissions implications: An overview. *Global Environmental Change*, *42*, 153–168.
919 https://doi.org/10.1016/j.gloenvcha.2016.05.009
920
921 Sato, T., Kimura, F., & Kitoh, A. (2007). Projection of global warming onto regional
922 precipitation over Mongolia using a regional climate model. *Journal of Hydrology*,
923 *333*(1), 144–154. https://doi.org/10.1016/j.jhydrol.2006.07.023
924
925 Schär, C., Frei, C., Lüthi, D., & Davies, H. C. (1996). Surrogate climate-change scenarios for
926 regional climate models. *Geophysical Research Letters*, *23*(6), 669–672.
927 https://doi.org/10.1029/96gl00265
928
929 Schumacher, R. S., & Peters, J. M. (2017). Near-Surface Thermodynamic Sensitivities in
930 Simulated Extreme-Rain-Producing Mesoscale Convective Systems. *Monthly Weather*
931 *Review*, 145(6), 2177–2200. https://doi.org/10.1175/mwr-d-16-0255.1
932
933 Schwab, D. J., Leshkevich, G. A., & Muhr, G. C. (1992). Satellite Measurements of Surface
934 Water Temperature in the Great Lakes: Great Lakes Coastwatch. *Journal of Great Lakes*
935 *Research*, *18*(2), 247–258. https://doi.org/10.1016/s0380-1330(92)71292-1
936
937 Scott, R. W., & Huff, F. A. (1996). Impacts of the Great Lakes on Regional Climate Conditions.
938 *Journal of Great Lakes Research*, *22*(4), 845–863. https://doi.org/10.1016/S0380-
939 1330(96)71006-7
940
941 Seeley, J. T., & Romps, D. M. (2015). The Effect of Global Warming on Severe Thunderstorms
942 in the United States. *Journal of Climate*, *28*(6), 2443–2458. https://doi.org/10.1175/JCLI-
943 D-14-00382.1
944
945 Seland, Ø., Bentsen, M., Oliviè, D. J. L., Toniazzo, T., Gjermundsen, A., Graff, L. S., et al.
946 (2020). Overview of the Norwegian Earth System Model (NorESM2) and key climate
947 response of CMIP6 DECK, historical, and scenario simulations. *Geoscientific Model*
948 *Development*, 13(12), 6165-6200. https://doi.org/10.5194/gmd-13-6165-2020.
949 Seo, D. J., & Breidenbach, J. P. (2002). Real-time correction of spatially nonuniform bias in
950 radar rainfall data using rain gauge measurements. *Journal of Hydrometeorology*, *3*(2),
951 93–111. https://doi.org/10.1175/1525-7541(2002)003<0093:rtcosn>2.0.co;2
952

Sharma, A., Hamlet, A. F., Fernando, H. J. S., Catlett, C. E., Horton, D. E., Kotamarthi, V. R., et al. (2018). The Need for an Integrated Land-Lake-Atmosphere Modeling System, Exemplified by North America's Great Lakes Region. *Earth's Future*, *6*(10), 1366–1379. https://doi.org/10.1029/2018EF000870

Sheffield, J., & Wood, E. F. (2008). Projected changes in drought occurrence under future global warming from multi-model, multi-scenario, IPCC AR4 simulations. *Climate Dynamics*, *31*(1), 79–105. https://doi.org/10.1007/s00382-007-0340-z

Shi, Q., & Xue, P. (2019). Impact of Lake Surface Temperature Variations on Lake Effect Snow Over the Great Lakes Region. *Journal of Geophysical Research: Atmospheres*, *124*(23), 12553–12567. https://doi.org/10.1029/2019JD031261

Shepherd, T. G. (2019). Storyline approach to the construction of regional climate change information. *Proceedings of the Royal Society A*, 475(2225), 20190013. https://doi.org/10.1098/rspa.2019.0013

Skamarock, W. C., Klemp, J. B., Dudhia, J., Gill, D. O., Barker, D. M., Duba, M. G., et al. (2008). A description of the advanced research WRF version 3, NCAR Technical Note. https://doi.org/10.5065/d68s4mvh

Swart, N. C., Cole, J. N. S., Kharin, V. V., Lazare, M., Scinocca, J. F., Gillett, N. P., et al. (2019). The Canadian earth system model version 5 (CanESM5. 0.3). *Geoscientific Model Development*, 12(11), 4823-4873. https://doi.org/10.5194/gmd-12-4823-2019.

Teutschbein, C., & Seibert, J. (2012). Bias correction of regional climate model simulations for hydrological climate-change impact studies: Review and evaluation of different methods. *Journal of Hydrology*, *456*, 12–29. https://doi.org/10.1016/j.jhydrol.2012.05.052

Thompson, G., Rasmussen, R. M., & Manning, K. (2004). Explicit Forecasts of Winter Precipitation Using an Improved Bulk Microphysics Scheme. Part I: Description and Sensitivity Analysis. *Monthly Weather Review*, *132*(2), 519–542. https://doi.org/10.1175/1520-0493(2004)132<0519:EFOWPU>2.0.CO;2

Thompson, G., Field, P. R., Rasmussen, R. M., & Hall, W. D. (2008). Explicit forecasts of winter precipitation using an improved bulk microphysics scheme. Part II: Implementation of a new snow parameterization. *Monthly Weather Review*, *136*(12), 5095–5115. https://doi.org/10.1175/2008mwr2387.1

Tidwell, V. C., & Pebbles, V. (2015). The Water-Energy-Environment Nexus in the Great Lakes Region: The Case for Integrated Resource Planning. *Energy and Environment Research*, *5*(2), 1. https://doi.org/10.5539/eer.v5n2p1

Trapp, R. J., Woods, M. J., Lasher-Trapp, S. G., & Grover, M. A. (2021). Alternative Implementations of the "Pseudo-Global-Warming" Methodology for Event-Based

Simulations. *Journal of Geophysical Research: Atmospheres*, *126*(24), e2021JD035017-e2021JD035017. https://doi.org/10.1029/2021jd035017

Trenberth, K. (2011). Changes in precipitation with climate change. *Climate Research*, *47*(1), 123–138. https://doi.org/10.3354/cr00953

Wang, J., Xue, P., Pringle, W., Yang, Z., & Qian, Y. (2022). Impacts of Lake Surface Temperature on the Summer Climate Over the Great Lakes Region. *Journal of Geophysical Research: Atmospheres*, *127*(11). https://doi.org/10.1029/2021JD036231

Wang, J., Qian, Y., Pringle, W., Chakraborty, T. C., Hetland, R., Yang, Z., & Xue, P. (2023). Contrasting effects of lake breeze and urbanization on heat stress in Chicago metropolitan area. *Urban Climate*, *48*, 101429. https://doi.org/10.1016/j.uclim.2023.101429

Workoff, T. E., Kristovich, D. A. R., Laird, N. F., Laplante, R., & Leins, D. (2012). Influence of the lake Erie overlake boundary layer on deep convective storm evolution. *Weather and Forecasting*, *27*(5), 1279–1289. https://doi.org/10.1175/waf-d-11-00076.1

Xue, P., Pal, J. S., Ye, X., Lenters, J. D., Huang, C., & Chu, P. Y. (2017). Improving the Simulation of Large Lakes in Regional Climate Modeling: Two-Way Lake–Atmosphere Coupling with a 3D Hydrodynamic Model of the Great Lakes. *Journal of Climate*, *30*(5), 1605–1627. https://doi.org/10.1175/JCLI-D-16-0225.1

Xue, P., Ye, X., Pal, J. S., Chu, P. Y., Kayastha, M. B., & Huang, C. (2022). Climate Projections over the Great Lakes Region: Using Two-way Coupling of a Regional Climate Model with a 3-D Lake Model. *Geoscientific Model Development Discussions*, *2022*, 1–37. https://doi.org/10.5194/gmd-2021-440

Yang, Z., Qian, Y., Xue, P., Wang, J., Chakraborty, T. C., Pringle, W. J., et al. (2023a). Moisture Sources of Precipitation in the Great Lakes Region: Climatology and Recent Changes. *Geophysical Research Letters*, *50*(5). https://doi.org/10.1029/2022gl100682

Yang, Z., Varble, A., Berg, L. K., Qian, Y., Tai, S.-L., Chen, J., et al. (2023b). Sensitivity of precipitation displacement of a simulated MCS to changes in land Surface conditions. *Journal of Geophysical Research: Atmospheres*, 128, e2022JD037642. https://doi.org/10.1029/2022JD037642

Zobel, Z., Wang, J., Wuebbles, D. J., & Kotamarthi, V. R. (2018). Analyses for High-Resolution Projections Through the End of the 21st Century for Precipitation Extremes Over the United States. *Earth's Future*, *6*(10), 1471–1490. https://doi.org/10.1029/2018EF000956